Journal of Scientific Computing, Vol. 25, No. 3, December 2005 (© 2005)
DOI: 10.1007/s10915-004-4795-3

Inverse Polynomial Reconstruction of Two Dimensional Fourier Images

Jae-Hun Jung[1,2] **and Bernie D. Shizgal**[1,3]

Received October 31, 2003; accepted (in revised form) April 23, 2004

The Gibbs phenomenon is intrinsic to the Fourier representation for discontinous problems. The inverse polynomial reconstruction method (IPRM) was proposed for the resolution of the Gibbs phenomenon in previous papers [Shizgal, B. D., and Jung, J.-H. (2003) and Jung, J.-H., and Shizgal, B. D. (2004)] providing spectral convergence for one dimensional global and local reconstructions. The inverse method involves the expansion of the unknown function in polynomials such that the residue between the Fourier representations of the final representation and the unknown function is orthogonal to the Fourier or polynomial spaces. The main goal of this work is to show that the one dimensional inverse method can be applied successfully to reconstruct two dimensional Fourier images. The two dimensional reconstruction is implemented globally with high accuracy when the function is analytic inside the given domain. If the function is piecewise analytic and the local reconstruction is sought, the inverse method is applied slice by slice. That is, the one dimensional inverse method is applied to remove the Gibbs oscillations in one direction and then it is applied in the other direction to remove the remaining Gibbs oscillations. It is shown that the inverse method is exact if the two-dimensional function to be reconstructed is a piecewise polynomial. The two-dimensional Shepp–Logan phantom image of the human brain is used as a preliminary study of the inverse method for two dimensional Fourier image reconstruction. The image is reconstructed with high accuracy with the inverse method.

KEY WORDS: Gibbs phenomenon; Fourier approximation; Inverse polynomial reconstruction method; Two-dimensional image reconstruction; Shepp–Logan phantom image.

[1] Institute of Applied Mathematics, University of British Columbia, Vancouver, British Columbia, Canada, V6T 1Z1.
[2] Pacific Institute for the Mathematical Sciences, University of British Columbia, 1933 West Mall,Vancouver, B.C., Canada, V6T 1Z2. E-mail: jung@iam.ubc.ca
[3] Department of Chemistry, University of British Columbia, 2036 Main Mall, Vancouver, B.C., Canada, V6T 1Z1.

1. INTRODUCTION

For most physical or engineering applications, Fourier functions are commonly used to reconstruct a desired function from the finite set of data especially in signal processing and image reconstruction [13,27]. Such Fourier representations occur in a wide range of applications such as cartography of planetary images, and remote sensing of the Earth, the reconstruction of astronomical images, chromosome karyotyping and computer tomographic (CT) image reconstruction in medical applications [8, 20–22,26]. Reconstruction with Fourier functions yields so-called spectral convergence if the function is periodic and smooth in the given domain. However, in the case that the function or its derivatives are no longer periodic or smooth, the Fourier representation suffers from Gibbs oscillations in the neighborhood of a discontinuity [15,16,24,25]. The contamination of the reconstructed function by Gibbs oscillations is common in applications such as in signal processing or image reconstruction problems [9, 24,26,28]. For example, satellite images are usually a collection of many individual Fourier images. To restore the entire global image of the object, the individual local images have to be patched properly. This global image mapping is usually required owing to the large scale of the object. Planetary image mapping such as the global mapping of the Martian surface is one such example [20,21]. When the individual Fourier images are collaged in this way, discontinuities arise at the boundaries of each individual frame resulting in the contamination of the final image due to the Gibbs oscillations. The reconstruction of medical images is also a good example of the Gibbs oscillations. A typical case is the CT image of the human brain. In the CT cerebral image, we clearly see the huge jumps of the image at the skull bone boundaries and at the boundaries made by the cerebral cortexes of interior sub-components [24,28]. In the neighborhood of these jumps, the Fourier image is considerably contaminated by the Gibbs oscillations.

A widely used technique for reducing the effects of the Gibbs oscillations is to filter out the higher Fourier modes [4,13,14]. However, since the Fourier functions are still used for the reconstruction of the image, its convergence remains only $O(1)$ in the neighborhood of the discontinuity. In order to obtain rapid convergence better than $O(1)$ over the entire domain, various algorithms have been developed. Among them, methods using spectral molifiers was introduced in Gottlieb and Tadmor [18] and has been developed in Tadmor and Tanner [31]. Methods using non-periodic basis sets such as rational functions [7] or Gegenbauer polynomials have also been developed [16,17]. Other methods are described in the references cited therein. Recently a new efficient and robust algorithm was

developed referred to as the Inverse Polynomial Reconstruction Method (IPRM) [23,30] inspired by the Gegenbauer reconstruction method formulated by Gottlieb and coworkers [16,17]. The IPRM relies on the polynomial re-expansion of the unknown function, and requires that the residue between the Fourier representations of the sought polynomial and the unknown function be orthogonal to the Fourier or polynomial spaces. The IPRM achieves an exact reconstruction if the unknown function is a polynomial. In the previous papers [23,30], the global and local reconstruction in one dimension with the IPRM was illustrated for arbitrary analytic functions, showing spectral convergence and exact resolution for polynomial functions. It is also shown that the final polynomial representation with the IPRM is unique regardless of the basis set chosen. That is, one can use any polynomial basis set.

In this paper, we extend the results of the previous studies to the global and local two-dimensional (2D) image reconstruction with the IPRM as a preliminary study of the IPRM for image reconstruction. We show that the 1D IPRM is extended straightforwardly to the 2D IPRM. As with the 1D IPRM, the 2D IPRM also provides an exact reconstruction if the function to be reconstructed is a piecewise polynomial. As with other reconstruction methods, the IPRM for image reconstruction requires a high order edge detection algorithm when the local reconstruction is formulated. Thus the edge location detection algorithm should be carefully addressed with the reconstruction method being used. Edges are common discontinuities in the medical images as in the CT brain images. Once the exact locations of edges are known, the IPRM provides spectral convergence of 2D images. In general, however, the exact edge locations are not easily determined and, therefore it might not be able to remove the edge effects completely from the reconstructed images. In this paper, however, it is not our intention to provide edge detection algorithms, and we regard the exact edge locations as given. We use the exact data on a discrete grid and reconstruct the image in arbitrary points. By using the exact data set and the proper definition of the edge, we reconstruct the Shepp–Logan phantom image with the IPRM. The reconstruction of the phantom image with the IPRM is exact if the exact Fourier coefficients are known, and the overall image is reconstructed with high accuracy.

In Sec. 2, the 1D IPRM is briefly described. In Sec. 3, the 2D global reconstruction with the IPRM is explained. In Sec. 4 the local reconstruction of sub-domains is shown. It is also shown that the 2D reconstruction of the piecewise polynomial images is exact when the unknown function is a piecewise polynomial. In Sec. 5, the Shepp–Logan phantom image is reconstructed with the IPRM with high accuracy and the issues of the

edge effects are discussed. In Sec. 6, we briefly address the remaining problems of the IPRM for the 2D image reconstructions.

2. THE INVERSE POLYNOMIAL RECONSTRUCTION METHOD

Gottlieb and Shu [16] have developed the Gegenbauer reconstruction method extensively. The main idea of the Gegenbauer reconstruction method is to use the eigenfunctions of the singular Sturm–Liouville equations that are non-periodic instead of the Fourier functions that are periodic in order to reconstruct the function. In fact, the expansion of the original analytic function in such non-periodic polynomials yields spectral accuracy over the entire domain. Inspired by this fact, the IPRM seeks a reconstruction as a polynomial, and it recovers the function with spectral accuracy as the expansion of the original function in the polynomial basis set is spectrally accurate. Detailed discussions of the IPRM were provided in the previous papers [30,23]. In the previous papers, it is shown that the reconstruction with the IPRM is exact independent of the basis sets being used if the function to be reconstructed is a polynomial. For example, if one uses Gegenbauer polynomials as a basis set, the IPRM is λ-independent. It is also shown that the final representation with the IPRM is unique regardless of the basis sets for any analytic function to be reconstructed.

The 1D IPRM proceeds as follows. Let $f(x)$ be the unknown function and $f_N(x)$ its Fourier approximation of degree of $2N$ on the Fourier space $\mathbf{F}_N = \text{span}\ \{\exp(\text{i}k\pi x) | -N \leqslant k \leqslant N\}$ in $x \in [-1, 1]$ such that

$$f_N(x) = \sum_{k=-N}^{N} \hat{f}_k \exp(\text{i}k\pi x), \tag{1}$$

where the Fourier coefficients $\hat{f}_k$ are given as

$$\hat{f}_k = \frac{1}{2}\int_{-1}^{1} f(x)\exp(-\text{i}k\pi x)dx \equiv (f(x), \exp(\text{i}k\pi x))_F, \tag{2}$$

where the parenthesis $(\cdot,\cdot)_F$ denotes the inner product. We seek a reconstructed function $\tilde{f}_m(x)$ as a polynomial of degree m such that

$$\tilde{f}_m(x) = \sum_{l=0}^{m} \tilde{g}_l C_l^{\lambda}(x), \tag{3}$$

where $C_l^{\lambda}(x)$ can be any polynomial function of degree l with or without a parameter λ. Here we assume that $f(x)$ is analytic inside the given domain

and thus $f(x)$ has a polynomial representation such as

$$f(x) = \sum_{l=0}^{\infty} g_l C_l^{\lambda}(x). \tag{4}$$

This polynomial set can be orthogonal or non-orthogonal polynomials such as the Gegenbauer polynomials [5,10,17] or the primitive polynomials [23]. In the previous papers, we have used the Gegenbauer polynomials $C_l^{\lambda}(x)$ as the basis functions and in this work we prefer using Gegenbauer polynomials for consistency with our previous works. The Gegenbauer polynomials $C_l^{\lambda}(x)$ are defined as [3,19]

$$\frac{1}{h_l^{\lambda}} \int_{-1}^{1} (1-x^2)^{\lambda-\frac{1}{2}} C_l^{\lambda}(x) C_{l'}^{\lambda}(x) = \delta_{ll'}, \tag{5}$$

where h_l^{λ} is the normalization factor given by

$$h_l^{\lambda} = \sqrt{\pi} C_l^{\lambda}(1) \frac{\Gamma(\lambda+\frac{1}{2})}{\Gamma(\lambda)(l+\lambda)}. \tag{6}$$

The reconstruction problem with the IPRM can be stated as follows: *Find $\tilde{g}_l$ such that the residue $E(x)$ between the Fourier representations of $\tilde{f}_m(x)$ and $f(x)$ are minimized.* The residue is defined as

$$E(x) = f_N(x) - \tilde{f}_m^N(x), \tag{7}$$

where $\tilde{f}_m^N(x)$ is the Fourier representation of $\tilde{f}_m(x)$, that is,

$$\tilde{f}_m^N(x) = \sum_{k=-N}^{N} (\tilde{f}_m(x), \exp(\mathrm{i}k\pi x))_F \exp(\mathrm{i}k\pi x). \tag{8}$$

This minimization is done by making the residue orthogonal to the Fourier or polynomial spaces. In the previous paper [23], it is shown that making the residue orthogonal to any space is equivalent to it being orthogonal to the Fourier space, that is, $\tilde{g}_l$ is uniquely determined by

$$(E(x), \exp(\mathrm{i}k\pi x))_F = 0, \quad \forall k \in [-N, N]. \tag{9}$$

This can be easily done by equating $\tilde{f}_m^N(x)$ with the Fourier representation $f_N(x)$ of the original unknown function $f(x)$ and then by projecting each side to the Fourier space. Using the orthogonality of the Fourier functions and Eq. (9), we obtain

$$(\tilde{f}_m(x), \exp(\mathrm{i}k\pi x))_F = \hat{f}_k. \tag{10}$$

The matrix element W_{kl} of the transformation matrix $\mathbf{W}$ from the Gegenbauer space to the Fourier space is defined as

$$W_{kl} = \frac{1}{2}\int_{-1}^{1} C_l^{\lambda}(x)\exp(-\mathrm{i}k\pi x)dx = \left(C_l^{\lambda}(x), \exp(\mathrm{i}k\pi x)\right)_F. \tag{11}$$

With this definition of $\mathbf{W}$, Eq. (10) becomes

$$\sum_{l=0}^{m} W_{kl}\tilde{g}_l = \hat{f}_k. \tag{12}$$

By choosing the polynomial order m such that the transformation matrix $\mathbf{W}$ is a square matrix, that is, $m = 2N$, the IPRM determines $\tilde{g}_l$ by inverting $\mathbf{W}$, a non-singular matrix [23]. With the vector notations, $\tilde{\mathbf{g}} = (\tilde{g}_0, ..., \tilde{g}_m)^{\mathrm{T}}$, and $\hat{\mathbf{f}} = (\hat{f}_{-N}, ..., \hat{f}_N)^{\mathrm{T}}$, where the superscript T denotes the transpose, the IPRM is simply expressed by

$$\tilde{\mathbf{g}} = \mathbf{W}^{-1}\cdot\hat{\mathbf{f}}. \tag{13}$$

In the above equation, the transformation matrix $\mathbf{W}$ is a function of λ and thus so is $\tilde{\mathbf{g}}$ while $\hat{\mathbf{f}}$ is not. However, we note here that the final representation by the inverse method is λ-independent which has been shown in Jung and Shizgal [23] for the 1D case. For the 2D case, this is shown in the next section. Thus even though $\lambda \longrightarrow \infty$, the IPRM is well-defined and still has a unique representation. Moreover there is no other constraint on m for spectral convergence. In Ref. [23] it has been shown that if m increases, the error in the maximum norm converges spectrally. Thus if $m \longrightarrow \infty$, the maximum norm theoretically vanishes. Define the matrix $\mathbf{W}^{\perp}$ and the column vectors $\mathbf{g}$, and $\mathbf{g}^{\perp}$ such that

$$\mathbf{W}^{\perp} = [W_{kl}], \quad -N \leqslant k \leqslant N, \quad l \geqslant m+1, \tag{14}$$

and $\mathbf{g} = (g_0, g_1, \ldots, g_m)^{\mathrm{T}}$, and $\mathbf{g}^{\perp} = \lim_{i\to\infty}(g_{m+1}, g_{m+2}, \ldots, g_i)^{\mathrm{T}}$. Since

$$\hat{f}_k = \left(\sum_{l_x=0}^{m} g_l C_l^{\lambda}(x), \exp(\mathrm{i}k\pi x)\right)_F + \left(\sum_{l_x=m+1}^{\infty} g_l C_l^{\lambda}(x), \exp(\mathrm{i}k\pi x)\right)_F \tag{15}$$

from Eq. (13) we obtain

$$\mathbf{W}\cdot\tilde{\mathbf{g}} = \mathbf{W}\cdot\mathbf{g} + \mathbf{W}^{\perp}\cdot\mathbf{g}^{\perp}. \tag{16}$$

Thus

$$\mathbf{W}\cdot(\mathbf{g} - \tilde{\mathbf{g}}) + \mathbf{W}^{\perp}\cdot\mathbf{g}^{\perp} = 0. \tag{17}$$

If $f(x)$ is a polynomial of degree m, we have $\mathbf{g}^{\perp} = \mathbf{0}$, and thus we get

$$\mathbf{g} = \tilde{\mathbf{g}}. \tag{18}$$

Thus even though $m \to \infty$, we always have $\mathbf{g} = \tilde{\mathbf{g}}$. For this reason, one can increase m arbitrarily large even in the case the function to be reconstructed is a polynomial as in the examples in the later sections. However, in practice m cannot become infinite because the numerical evaluation of the transformation matrix $\mathbf{W}$ and its inversion should be done with finite-precision [12]. In Ref. [23] the round-off error effects have been discussed.

The main properties of the IPRM are briefly summarized in the following [23]:

- *Existence:* the transformation matrix $\mathbf{W}$ is non-singular and thus invertible
- *Exactness:* the IPRM is exact if the function to be reconstructed is a polynomial
- *Uniqueness:* the polynomial reconstruction with the IPRM is uniquely determined regardless of the basis functions used for any arbitrary analytic function to be reconstructed
- *Convergence:* the IPRM yields spectral convergence

3. 2D GLOBAL RECONSTRUCTION WITH THE IPRM

3.1. Exactness and Uniqueness

The 2D reconstruction with the IPRM follows the discussion in Sec. 2 on the 1D IPRM straightforwardly. For simplicity, we consider a 2D rectangular domain $\Omega = [-1, 1]^2$, and we assume that $f(x, y)$ is analytic in Ω but not necessarily periodic. The Fourier approximation $f_N(x, y)$ of $f(x, y)$ is then given by

$$f_N(x, y) = \sum_{k_x=-N_x}^{N_x} \sum_{k_y=-N_y}^{N_y} \hat{f}_{k_x k_y} \mathrm{e}^{\mathrm{i}\pi(k_x x + k_y y)}, \tag{19}$$

where the Fourier coefficients $\hat{f}_{k_x k_y}$ are given by

$$\hat{f}_{k_x k_y} = \frac{1}{4} \int_{-1}^{1} \int_{-1}^{1} f(x, y) \mathrm{e}^{-\mathrm{i}\pi(k_x x + k_y y)} dx dy. \tag{20}$$

The number of the Fourier modes are $2N_x + 1$ and $2N_y + 1$ in the x and y variables, respectively. The finite Gegenbauer approximation $\tilde{f}_m(x, y)$ is

defined as

$$\tilde{f}_{m_x m_y}(x, y) = \sum_{l_x=0}^{m_x} \sum_{l_y=0}^{m_y} \tilde{g}_{l_x l_y} C_{l_x}^{\lambda}(x) C_{l_y}^{\lambda}(y). \tag{21}$$

Let $\tilde{f}_{m_x m_y}^{N}(x, y)$ be the Fourier representation of $\tilde{f}_{m_x m_y}(x, y)$ of degree $2N_x$ and $2N_y$. As with the 1D IPRM, the 2D IPRM defines the residue function as $E(x, y) = f_N(x, y) - \tilde{f}_{m_x m_y}^{N}(x, y)$. By making $E(x, y)$ orthogonal to the Fourier space and using the orthogonality of the Fourier functions, we obtain

$$\frac{1}{4} \sum_{l_x=0}^{m_x} \sum_{l_y=0}^{m_y} \tilde{g}_{l_x l_y} \int_{-1}^{1} C_{l_x}^{\lambda}(x) e^{-i\pi k_x x} dx \int_{-1}^{1} C_{l_y}^{\lambda}(y) e^{-i\pi k_y y} dy = \hat{f}_{k_x k_y}. \tag{22}$$

Let the matrices $\hat{\mathbf{F}} = [\hat{f}_{k_x k_y}]$, $\tilde{\mathbf{G}} = [\tilde{g}_{l_x l_y}]$, $\mathbf{W}_x = [\frac{1}{2} \int_{-1}^{1} e^{-ik_x \pi x} C_{l_x}^{\lambda}(x) dx]$, and $\mathbf{W}_y = [\frac{1}{2} \int_{-1}^{1} e^{-ik_y \pi y} C_{l_y}^{\lambda}(y) dy]$. The above linear system, Eq. (22), can be rewritten in matrix form,

$$\mathbf{W}_x \cdot \tilde{\mathbf{G}} \cdot \mathbf{W}_y{}^{\mathrm{T}} = \hat{\mathbf{F}}. \tag{23}$$

Here note that all these matrices are not necessarily square matrices. By choosing $m_x = 2N_x$ and $m_y = 2N_y$ we can make $\mathbf{W}_x$ and $\mathbf{W}_y^{\mathrm{T}}$ square matrices and thus obtain $\tilde{\mathbf{G}}$ by the inversion of $\mathbf{W}_x$ and $\mathbf{W}_y^{\mathrm{T}}$ such that

$$\tilde{\mathbf{G}} = \mathbf{W}_x^{-1} \cdot \hat{\mathbf{F}} \cdot \mathbf{W}_y^{\mathrm{T}-1}. \tag{24}$$

Eq. (24) is the 2D analogue of the 1D inverse method, Eq. (13).

Remark 1. This 2D global inverse reconstruction is λ-independent for any two dimensional analytic function and the final representation is unique.

To show the λ-independence and the uniqueness suppose that we have two final representations $\tilde{f}_{mn}^{1}(x, y)$ and $\tilde{f}_{mn}^{2}(x, y)$ obtained with the 2D inverse reconstruction, Eq. (24), based on the Gegenbauer polynomials with λ_1 and λ_2, respectively, such that

$$\tilde{f}_{mn}^{1}(x, y) = \sum_{l_x=0}^{m} \sum_{l_y=0}^{n} \tilde{g}_{l_x l_y}(\lambda_1) C_{l_x}^{\lambda_1}(x) C_{l_y}^{\lambda_1}(y),$$

$$\tilde{f}_{mn}^{2}(x, y) = \sum_{l_x=0}^{m} \sum_{l_y=0}^{n} \tilde{g}_{l_x l_y}(\lambda_2) C_{l_x}^{\lambda_2}(x) C_{l_y}^{\lambda_2}(y).$$

The matrices $\tilde{\mathbf{G}}(\lambda_1) = [\tilde{g}_{l_x l_y}(\lambda_1)]$ and $\tilde{\mathbf{G}}(\lambda_2) = [\tilde{g}_{l_x l_y}(\lambda_2)]$ in these equations are

$$\begin{aligned} \tilde{\mathbf{G}}(\lambda_1) &= \mathbf{W}_x^{-1}(\lambda_1) \cdot \hat{\mathbf{F}} \cdot \mathbf{W}_y^{\mathrm{T}^{-1}}(\lambda_1), \\ \tilde{\mathbf{G}}(\lambda_2) &= \mathbf{W}_x^{-1}(\lambda_2) \cdot \hat{\mathbf{F}} \cdot \mathbf{W}_y^{\mathrm{T}^{-1}}(\lambda_2). \end{aligned} \tag{25}$$

Due to the uniqueness of polynomials we know that there exits a polynomial $p_{mn}(x, y)$ such that

$$\tilde{f}_{mn}^1(x, y) = p_{mn}(x, y), \tag{26}$$

and

$$p_{mn}(x, y) = \sum_{l_x=0}^{m} \sum_{l_y=0}^{n} s_{l_x l_y} C_{l_x}^{\lambda_2}(x) C_{l_y}^{\lambda_2}(y).$$

By projecting both sides of Eq. (26) onto the Fourier space, we obtain that

$$\mathbf{W}_x(\lambda_1) \cdot \tilde{\mathbf{G}}(\lambda_1) \cdot \mathbf{W}_y{}^{\mathrm{T}}(\lambda_1) = \mathbf{W}_x(\lambda_2) \cdot \mathbf{S} \cdot \mathbf{W}_y{}^{\mathrm{T}}(\lambda_2),$$

where $\mathbf{S} = [s_{l_x l_y}]$. Since $\mathbf{W}_x(\lambda_1) \cdot \tilde{\mathbf{G}}(\lambda_1) \cdot \mathbf{W}_y{}^{\mathrm{T}}(\lambda_1) = \hat{\mathbf{F}}$, Eq. (25), we obtain that,

$$\mathbf{W}_x(\lambda_2) \cdot \mathbf{S} \cdot \mathbf{W}_y{}^{\mathrm{T}}(\lambda_2) = \hat{\mathbf{F}}.$$

Thus

$$\mathbf{S} = \mathbf{W}_x^{-1}(\lambda_2) \cdot \hat{\mathbf{F}} \cdot \mathbf{W}_y^{\mathrm{T}^{-1}}(\lambda_2).$$

Recall that we already made $\mathbf{W}_x(\lambda_2)$ and $\mathbf{W}_y{}^{\mathrm{T}}(\lambda_2)$ square matrices in Eq. (25) and that they are non-singular. From Eq. (25), we thus have that

$$\mathbf{S} = \tilde{\mathbf{G}}(\lambda_2),$$

and hence from Eq. (26) we obtain that,

$$\tilde{f}_{mn}^1(x, y) = \tilde{f}_{mn}^2(x, y).$$

Thus the final 2D reconstruction with the inverse method is unique and independent of λ.

Remark 2. The 2D global inverse reconstruction is exact if the given function $f(x, y)$ is a polynomial.

We can easily show that the 2D inverse reconstruction is exact as is the 1D inverse reconstruction. Suppose that $f(x, y)$ is a polynomial of degree $m+n$ such that

$$f_{mn}(x, y) = \sum_{l_x=0}^{m} \sum_{l_y=0}^{n} g_{l_x l_y} C_{l_x}^{\lambda}(x) C_{l_y}^{\lambda}(y).$$

By taking $m = 2N_x$ and $n = 2N_y$, we have

$$\hat{\mathbf{F}} = \mathbf{W}_x \cdot \mathbf{G} \cdot \mathbf{W}_y^{\mathrm{T}},$$

where $\hat{\mathbf{F}}$ is $(m+1) \times (n+1)$ matrix and $\mathbf{W}_x$ and $\mathbf{W}_y$ are square matrices. By the definition of the 2D inverse reconstruction Eq. (24)

$$\tilde{\mathbf{G}}(\lambda) = \mathbf{G}(\lambda). \tag{27}$$

Thus we know that the 2D global inverse reconstruction is exact when the function is a polynomial.

3.2. Symmetry Considerations and Numerical Example

For the numerical experiments discussed later we split Eq. (24) into two parts by using the parity relation for the Gegenbauer polynomials,

$$C_l^{\lambda}(-x) = (-1)^l C_l^{\lambda}(x). \tag{28}$$

If we let $\mathbf{T}$ and $\mathbf{V}$ be the imaginary and real parts of $\mathbf{W}$, then the real part $\mathbf{V}$ of $\mathbf{W}$ vanishes if l is odd, and the imaginary part $\mathbf{T}$ of $\mathbf{W}$ vanishes if l is even. As in the one dimensional case, one can calculate the inversion directly or one can split the system using the symmetry Eq. (28). We first observe that all matrices except $\tilde{\mathbf{G}}$ are complex. Let the superscripts R and I denote the real and imaginary parts of the quantities. As done in the 1D case [23], we have

$$\begin{aligned} \mathbf{W}_x^R \cdot \tilde{\mathbf{G}} \cdot \mathbf{W}_y^{R\mathrm{T}} - \mathbf{W}_x^I \cdot \tilde{\mathbf{G}} \cdot \mathbf{W}_y^{I\mathrm{T}} &= \hat{\mathbf{F}}^R, \\ \mathbf{W}_x^R \cdot \tilde{\mathbf{G}} \cdot \mathbf{W}_y^{I\mathrm{T}} + \mathbf{W}_x^I \cdot \tilde{\mathbf{G}} \cdot \mathbf{W}_y^{R\mathrm{T}} &= \hat{\mathbf{F}}^I. \end{aligned} \tag{29}$$

With the definition of $\mathbf{V}$ and $\mathbf{T}$, we have that $\mathbf{W}_x = \mathbf{V}_x + \mathrm{i}\mathbf{T}_x$ and $\mathbf{W}_y = \mathbf{V}_y + \mathrm{i}\mathbf{T}_y$. Thus the above equations become

$$\begin{aligned} \mathbf{V}_x \cdot \tilde{\mathbf{G}} \cdot \mathbf{V}_y^{\mathrm{T}} - \mathbf{T}_x \cdot \tilde{\mathbf{G}} \cdot \mathbf{T}_y^{\mathrm{T}} &= \hat{\mathbf{F}}^R, \\ \mathbf{V}_x \cdot \tilde{\mathbf{G}} \cdot \mathbf{T}_y^{\mathrm{T}} + \mathbf{T}_x \cdot \tilde{\mathbf{G}} \cdot \mathbf{V}_y^{\mathrm{T}} &= \hat{\mathbf{F}}^I. \end{aligned} \tag{30}$$

At first sight, the two terms on the LHS of each equation appear not to be reduced to one term. However if we use the symmetries of $\mathbf{T}$ and $\mathbf{V}$, we can simplify the above systems. Since $\mathbf{V}$ and $\mathbf{T}$ have null elements for $l=$ even and $l=$ odd, respectively, $\mathbf{V}_x \cdot \tilde{\mathbf{G}} \cdot \mathbf{V}_y^{\mathrm{T}}$ can be decomposed by using only even rows and even columns of $\tilde{\mathbf{G}}$. Similarly, $\mathbf{T}_x \cdot \tilde{\mathbf{G}} \cdot \mathbf{T}_y^{\mathrm{T}}$ can be rewritten in terms of only odd rows and odd columns of $\tilde{\mathbf{G}}$, and $\mathbf{V}_x \cdot \tilde{\mathbf{G}} \cdot \mathbf{T}_y^{\mathrm{T}}$ and $\mathbf{T}_x \cdot \tilde{\mathbf{G}} \cdot \mathbf{V}_y^{\mathrm{T}}$ by only the cross terms of $\tilde{\mathbf{G}}$. We decompose $\tilde{\mathbf{G}}$ as

$$\tilde{\mathbf{G}} = \tilde{\mathbf{G}}^{\mathrm{ee}} + \tilde{\mathbf{G}}^{\mathrm{oo}} + \tilde{\mathbf{G}}^{\mathrm{eo}} + \tilde{\mathbf{G}}^{\mathrm{oe}}, \tag{31}$$

where the superscripts e and o denote even and odd rows or columns. By using this decomposition, the above systems become

$$\begin{aligned} \mathbf{V}_x \cdot \hat{\mathbf{G}}^{\mathrm{ee}} \cdot \mathbf{V}_y^{\mathrm{T}} - \mathbf{T}_x \cdot \hat{\mathbf{G}}^{\mathrm{oo}} \cdot \mathbf{T}_y^{\mathrm{T}} &= \hat{\mathbf{F}}^R, \\ \mathbf{V}_x \cdot \hat{\mathbf{G}}^{\mathrm{eo}} \cdot \mathbf{T}_y^{\mathrm{T}} + \mathbf{T}_x \cdot \hat{\mathbf{G}}^{\mathrm{oe}} \cdot \mathbf{V}_y^{\mathrm{T}} &= \hat{\mathbf{F}}^I. \end{aligned} \tag{32}$$

Furthermore using parity, we have that,

$$\begin{aligned} (\mathbf{V}_x + \mathbf{T}_x) \cdot (\hat{\mathbf{G}}^{\mathrm{ee}} - \hat{\mathbf{G}}^{\mathrm{oo}}) \cdot (\mathbf{V}_y^{\mathrm{T}} + \mathbf{T}_y^{\mathrm{T}}) &= \hat{\mathbf{F}}^R, \\ (\mathbf{V}_x + \mathbf{T}_x) \cdot (\hat{\mathbf{G}}^{\mathrm{eo}} + \hat{\mathbf{G}}^{\mathrm{oe}}) \cdot (\mathbf{T}_y^{\mathrm{T}} + \mathbf{V}_y^{\mathrm{T}}) &= \hat{\mathbf{F}}^I. \end{aligned} \tag{33}$$

With the assumption that a sufficient number of Fourier modes (N_x, N_y) are provided to resolve the original function $f(x, y)$, the number of the Gegenbauer modes (l_x, l_y) can be always taken less than $(2N_x, 2N_y)$. We use the Fourier modes only up to (m_x, m_y) such that $N_x = m_x/2$, and $N_y = m_y/2$. One can use the residue method to determine the proper choice of m_x and m_y [30]. Here again we note that in general m_x is different from m_y. With the choice of $(N_x, N_y) = (m_x/2, m_y/2)$, $\mathbf{V}_x + \mathbf{T}_x$, and $\mathbf{V}_y + \mathbf{T}_y$ become square matrices. Then we solve the linear system with

$$\begin{aligned} \tilde{\mathbf{G}}^{\mathrm{ee}} - \tilde{\mathbf{G}}^{\mathrm{oo}} &= (\mathbf{V}_x + \mathbf{T}_x)^{-1} \cdot \tilde{\mathbf{F}}^R \cdot (\mathbf{V}_y^{\mathrm{T}} + \mathbf{T}_y^{\mathrm{T}})^{-1}, \\ \tilde{\mathbf{G}}^{\mathrm{eo}} + \tilde{\mathbf{G}}^{\mathrm{oe}} &= (\mathbf{V}_x + \mathbf{T}_x)^{-1} \cdot \hat{\mathbf{F}}^I \cdot (\mathbf{V}_y^{\mathrm{T}} + \mathbf{T}_y^{\mathrm{T}})^{-1}. \end{aligned} \tag{34}$$

We illustrate the functioning of the 2D IPRM with its application to specific examples.

Example 1. We consider a simple example that was used by Gelb and Gottlieb [11], $f(x, y) = \mathrm{e}^{2.3i\pi x + 1.2i\pi y}$, $x \in [-1, 1]^2$. We use $2N + 1$ Fourier modes with $N = 4, 8$, and 16 for both x and y directions and use $m_x = m_y = 2N$. We use the Legendre polynomials as the basis polynomials, i.e., $\lambda = \frac{1}{2}$, for which the exact form of the transformation matrix $\mathbf{W}$ is known [3]. As shown in the previous papers [23,30], no conditions on λ

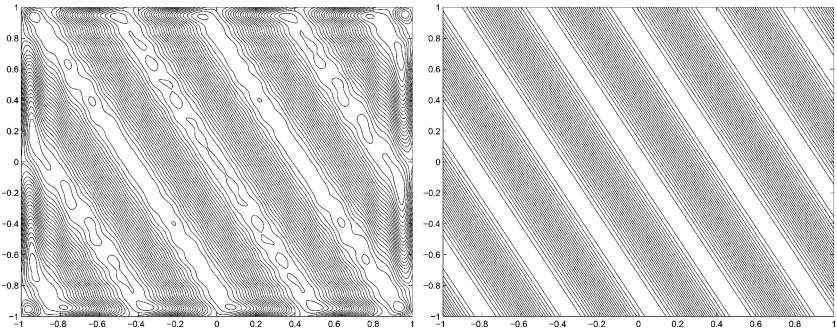

Fig. 1. Approximation of $f(x, y) = e^{2.3i\pi x + 1.2i\pi y}$ with the IPRM. Figure on the left shows the Fourier approximation of $f(x, y)$ with $N_x = N_y = N = 16$ and the figure on the right shows the reconstructed image with the IPRM and $m_x = m_y = 2N = 32$.

are imposed in order to obtain spectral convergence for the reconstructed function, and thus we can keep the same λ for all N. Moreover, we use the exact Fourier coefficients $\hat{f}_{k_x k_y}$ given by

$$\hat{f}_{k_x k_y} = \frac{1}{\pi^2} \sin(\pi(2.3 - k_x)) \sin(\pi(1.2 - k_y))/(2.3 - k_x)/(1.2 - k_y). \quad (35)$$

Since $\hat{f}_{k_x k_y}$ is real, all the cross terms of $\hat{\mathbf{G}}^{eo}$ and $\tilde{\mathbf{G}}^{oe}$ vanish and thus one has only non-vanishing $\tilde{\mathbf{G}}^{ee}$ and $\tilde{\mathbf{G}}^{oo}$ in Eqs. (33) and (34). To evalute the inversion of the transformation matrix, we use the MATLAB® built-in inversion function, *inv*. For the graphical representation of the results in Fig. 1, we use 400×400 grid points.

As shown in Fig. 1 the Gibbs oscillations near neighborhoods of the domain boundaries shown in the Fourier image (left) are considerably reduced with the IPRM (right). In Table I, the maximum pointwise absolute error is shown versus N and demonstrates that the IPRM provides a very accurate result.

Table I. Absolute Maximum Error of $f(x, y)$ with the IPRM

N	m	Error
4	8	2.9842
8	16	1.4578E-03
16	32	6.7740E-09

4. LOCAL RECONSTRUCTION WITH THE IPRM

In most cases, the function $f(x, y)$ to be reconstructed or its derivatives can be non-smooth and has many jumps inside the given domain Ω. This yields the severe oscillatory approximations in the neighboohood of such jumps. For the reconstruction, we seek a piecewise smooth function by splitting Ω into multiple subdomains. In this work, we assume that the exact locations of the edges are known a priori. In Sec. 5, we discuss issues related to the edge effects when the IPRM is applied to the case that $f(x, y)$ is given only on a set of discrete grid points. In this section, we will briefly explain the 1D local inverse method and extend the method to the 2D local reconstruction. The extension of the 1D inverse method to 2D is here considered as the tensor product of the 1D case. However, the method can be singular even for subdomains with a simple geometry. Instead of reconstructing the 2D Fourier image in a global manner, we apply the 1D inverse method for a particular slice of the image in either the x-direction or the y-direction. By reconstructing the 2D Fourier image slice by slice, we achieve a higly accurate 2D reconstruction. When the function is a piecewise polynomial, the reconstruction is exact.

4.1. Multidomain 1D IPRM

In this section, we briefly explain the 1D local IPRM. Consider the one-dimensional function $f(x)$. Suppose that the exact locations of the edges are known and the sub-domains are well-defined such that

$$\Omega = [-1, 1] = \bigcup_{i=1}^{N_s} \Omega_i,$$

and

$$f(\Omega) = \bigoplus_{i=1}^{N_s} f_i(\Omega_i),$$

where N_s is the total number of the sub-domains and the subscript (or superscript) i denotes the ith sub-domain. Here let $\bigoplus$ denote that $f(\Omega)$ is the collection of $f_i(\Omega_i)$, such that

$$f(x) = f_i(x), \quad x \in \Omega_i,$$

and $\Omega_i \bigcap \Omega_j = \emptyset$ if $i \neq j$. Since we seek a piecewise smooth $f(x)$ and we approximate $f_i(x)$ as a finite Gegenbauer sum in each Ω_i, we let

$$\tilde{f}_i(x) = \sum_{l=0}^{\infty} \tilde{g}_l^i C_l^{\lambda}(X_i(x)), \quad x \in \Omega_i, \tag{36}$$

where $X_i(x)$ is the linear map such that

$$X_i(x) \to \xi \in [-1, 1], \quad x \in \Omega_i. \tag{37}$$

The Fourier coefficients $\hat{f}_k$ of $f(x)$ are given by

$$\begin{aligned} \hat{f}_k &= \sum_{i=1}^{N_s} \sum_{l=0}^{\infty} \tilde{g}_l^i \frac{1}{2} \int_{\Omega_i} C_l^{\lambda}(X_i(x)) \exp(-ik\pi x) dx \\ &= \sum_{i=1}^{N_s} \sum_{l=0}^{\infty} \tilde{g}_l^i \frac{1}{2} \int_{-1}^{1} C_l^{\lambda}(\xi) \exp(-ik\pi X_i^{-1}(\xi)) J_{\xi}^i d\xi, \end{aligned} \tag{38}$$

where J_{ξ}^i is the Jacobian such that $J_{\xi}^i = \frac{dX_i^{-1}(\xi)}{d\xi}$. We define the matrix element W_{kl}^i of the matrix $\mathbf{W}^i$ as

$$W_{kl}^i = \frac{1}{2} \int_{-1}^{1} C_l^{\lambda}(\xi) \exp(-ik\pi X_i^{-1}(\xi)) J_{\xi}^i d\xi. \tag{39}$$

Then by truncating the sum in Eq. (36) at N_s we have that

$$\sum_{i=1}^{N_s} \mathbf{W}^i \cdot \tilde{\mathbf{G}}^i = \hat{\mathbf{f}}, \tag{40}$$

where $\tilde{\mathbf{G}}^i = (\tilde{g}_0^i, \ldots, \tilde{g}_{m_i}^i)^{\mathrm{T}}$, and $\hat{\mathbf{f}} = (\hat{f}_{-N}, \ldots, \hat{f}_N)^{\mathrm{T}}$. Since the resolution is different for each $f_i(x)$, we note that each $\mathbf{W}^i$ has a different size although the number of its row vectors is equal to $2N+1$. By choosing the resolution properly with the constraint

$$\sum_{i=1}^{N_s} (1 + m_i) = 2N + 1,$$

and defining the matrix W as

$$\mathbf{W} = [\mathbf{W}^1 | \cdots | \mathbf{W}^{N_s}], \tilde{\mathbf{G}} = \begin{pmatrix} \tilde{\mathbf{G}}^1 \\ \vdots \\ \tilde{\mathbf{G}}^{N_s} \end{pmatrix}, \tag{41}$$

the complete reconstruction is given by Shizgal and Jung [30],

$$\tilde{\mathbf{G}} = \mathbf{W}^{-1} \cdot \hat{\mathbf{f}}. \tag{42}$$

Eq. (42) is the 1D multidomain version of the single domain inverse method given by Eq. (13).

Remark 3. One can show that each column of the matrix **W** is linearly independent and thus **W** is invertible. However, if Ω_i is made sufficiently small the calculation of **W** suffers from severe round off error and **W** is almost 'singular' numerically.

Remark 4. If $f(x)$ is a piecewise polynomial the inverse method is exact.

To prove the remark, suppose that the number of Fourier modes is enough to recover the original function and $f_i(x)$ in the ith subdomain is a polynomial of degree m_i. The vector $\hat{\mathbf{f}}$ whose components are the first $2N+1$ Fourier coefficients is given by,

$$\hat{\mathbf{f}} = \mathbf{W} \cdot \mathbf{G},$$

where **W** and **G** are defined in the same manner as Eq. (41) and the elements of **G** are composed of the exact expansion coefficients of $f_i(x)$. Since **W** is square and non-singular, we obtain

$$\mathbf{G} = \mathbf{W}^{-1} \cdot \hat{\mathbf{f}}.$$

This equation is exactly the same as Eq. (42). Thus we have

$$\tilde{\mathbf{G}}(\lambda) = \mathbf{G}(\lambda).$$

4.2. 2D Local Reconstruction

In this section, we investigate two methods for the 2D Fourier image reconstruction based on the 1D local inverse method. The first method is to reconstruct the 2D image domain-by-domain as discussed in Sec. 4.2.1. The domain-by-domain approach is straightforward and can be implemented easily. If the geometry of the subdomains is simple enough and the transformation matrix **W** is well defined, then the inverse method reconstructs $f(x, y)$ in an efficient way with high accuracy. However, in general this reconstruction is not either practical nor even possible despite its simplicity since (1) the geometry of each sub-domain defined by the edges is not always simple and thus **W** is not easy to calculate and (2) even for a simple geometry the transformation matrix **W** can be singular as shown later.

The second approach is to reconstruct the 2D image slice-by-slice. This method applies the 1D IPRM in one direction first to remove the Gibbs oscillations in that particular direction. Then the method applies

the 1D IPRM in the other direction to remove the Gibbs oscillations that remain. Compared to the domain-by-domain method, this method is computationally more expensive. However, as shown in the next section this slice-by-slice method is well-posed and yields accurate results as the transformation matrices involved in the reconstruction are always non-singular as in the 1D case.

In the following subsections, we first consider the 2D IPRM domain-by-domain which can be used only in the special case that the geometry is simple so that the transformation matrices **W** are not singular. Then we consider the slice-by-slice reconstruction method in Sec. 4.2.2.

4.2.1. Multidomain 2D IPRM

As done in the previous section for the 1D problem, we assume that the exact location of the edges are known and also assume that the function $f(x, y)$ is analytic in each domain. Let N_s be the total number of subdomains such that

$$f(\Omega) = \bigoplus_{i=1}^{N_s} f_i(\Omega_i), \quad \Omega = \bigcup_{i=1}^{N_s} \Omega_i, \tag{43}$$

and

$$\tilde{f}_i(x, y) = \sum_{l_x=0}^{\infty} \sum_{l_y=0}^{\infty} \tilde{g}^i_{l_x l_y} C^{\lambda}_{l_x}(X_i(x)) C^{\lambda}_{l_y}(Y_i(y)), \quad x, y \in \Omega_i, \tag{44}$$

where X_i and Y_i are the linear transformations such that

$$X_i(x) \longrightarrow \xi \in [-1, 1], \quad Y_i(y) \longrightarrow \eta \in [-1, 1] \quad (x, y) \in \Omega_i. \tag{45}$$

The Fourier coefficients $\hat{f}_{k_x k_y}$ are given for $(x, y) \in \Omega_i$ by

$$\begin{aligned}
\hat{f}_{k_x k_y} &= \frac{1}{4} \sum_{i=1}^{N_s} \sum_{l_x=0}^{\infty} \sum_{l_y=0}^{\infty} \tilde{g}^i_{l_x l_y} \int \int C^{\lambda}_{l_x}(X_i(x)) C^{\lambda}_{l_y}(Y_i(y)) \mathrm{e}^{-\mathrm{i}k_x \pi x} \mathrm{e}^{-\mathrm{i}k_y \pi y} dx\ dy \\
&= \frac{1}{4} \sum_{i=1}^{N_s} \sum_{l_x=0}^{\infty} \sum_{l_y=0}^{\infty} \tilde{g}^i_{l_x l_y} \int_{-1}^{1} C^{\lambda}_{l_x}(\xi) \mathrm{e}^{-\mathrm{i}k_x \pi X_i^{-1}(\xi)} J^i_{\xi} d\xi \\
&\quad \times \int_{-1}^{1} C^{\lambda}_{l_y}(\eta) \mathrm{e}^{-\mathrm{i}k_y \pi Y_i^{-1}(\eta)} J^i_{\eta} d\eta
\end{aligned}$$

where J^i_{ξ} and J^i_{η} are the Jacobians such that $J^i_{\xi} = \frac{dX_i^{-1}(\xi)}{d\xi}$ and $J^i_{\eta} = \frac{dY_i^{-1}(\xi)}{d\eta}$. We define the matrix $\mathbf{W}^i_x$ whose $k_x th$ row and $l_x th$ column element is given

by

$$\frac{1}{2}\int_{-1}^{1} C_{l_x}^{\lambda}(\xi)\mathrm{e}^{-\mathrm{i}\pi k_x X_i^{-1}(\xi)} J_{\xi}^{i} d\xi$$

and similarly the matrix $\mathbf{W}_y^i$ with the element given by

$$\frac{1}{2}\int_{-1}^{1} C_{l_y}^{\lambda}(\eta)\mathrm{e}^{-\mathrm{i}\pi k_y Y_i^{-1}(\eta)} J_{\eta}^{i} d\eta.$$

By truncating the Gegenbauer sums over l_x and l_y at m_x^i and m_y^i, respectively we have that

$$\hat{\mathbf{F}} = \sum_{i=1}^{N_\mathrm{s}} \mathbf{W}_x^i \cdot \tilde{\mathbf{G}}^i \cdot [\mathbf{W}_y^i]^\mathrm{T}, \tag{46}$$

where $\mathbf{W}_x^i$ is a k_x by m_x^i matrix, $\tilde{\mathbf{G}}^i$ a m_x^i by m_y^i matrix and $[\mathbf{W}_y^i]^\mathrm{T}$ a m_y^i by k_y matrix. The matrix $\hat{\mathbf{F}}$ is the matrix of Fourier coefficients defined by Eq. (20). Here m_x^i and m_y^i are the maximum order of Gegenbauer polynomials in x and y variables respectively in the ith interval. In order to find $\tilde{\mathbf{G}}^i$, one finds either $\mathbf{W}_x^i \cdot \tilde{\mathbf{G}}^i$ or $\tilde{\mathbf{G}}^i \cdot [\mathbf{W}_y^i]^\mathrm{T}$ first by inverting (46) and then finds $\tilde{\mathbf{G}}^i$ by inverting each sub-block of the resulting equation. As an example let us first find $\tilde{\mathbf{G}}^i \cdot [\mathbf{W}_y^i]^\mathrm{T}$. For this, we define matrices $\mathbf{W}_x$, and $\mathbf{R}$ such as

$$\mathbf{W}_x = \left[\mathbf{W}_x^1 | \mathbf{W}_x^2 | \cdot | \cdot | \cdot | \mathbf{W}_x^{N_\mathrm{s}}\right],$$
$$\mathbf{R} = \begin{bmatrix} \tilde{\mathbf{G}}^1 \cdot [\mathbf{W}_y^1]^\mathrm{T} \\ \tilde{\mathbf{G}}^2 \cdot [\mathbf{W}_y^2]^\mathrm{T} \\ \vdots \\ \tilde{\mathbf{G}}^{N_\mathrm{s}} \cdot [\mathbf{W}_y^{N_\mathrm{s}}]^\mathrm{T} \end{bmatrix}. \tag{47}$$

Then Eq. (46) becomes

$$\mathbf{W}_x \cdot \mathbf{R} = \hat{\mathbf{F}}. \tag{48}$$

In order to invert $\mathbf{W}_x$ we choose the maximum Gegenbauer polynomial order m_x^i of the ith interval such that

$$(m_x^1 + 1) + (m_x^2 + 1) + \cdots + (m_x^{N_x} + 1) = 2N_x + 1 \tag{49}$$

making $\mathbf{W}_x$ a square matrix. By inverting Eq. (48) we have that

$$\mathbf{R} = \mathbf{W}_x^{-1} \cdot \hat{\mathbf{F}}. \tag{50}$$

Let $\mathbf{A}[a:b]$ denote the matrix composed of the row vectors of the matrix $\mathbf{A}$ from the ath row to the bth row. With the definition of $\mathbf{R}$ in Eq. (47), one can find each $\tilde{\mathbf{G}}^i$ by comparing the sub-blocks of each matrix in the above equation such that

$$\begin{aligned}
\tilde{\mathbf{G}}^1 \cdot [\mathbf{W}_y^1]^{\mathrm{T}} &= \mathbf{R}[1 : m_x^1 + 1] = \mathbf{W}_x^{-1} \cdot \hat{\mathbf{F}}[1 : m_x^1 + 1] \\
\tilde{\mathbf{G}}^2 \cdot [\mathbf{W}_y^2]^{\mathrm{T}} &= \mathbf{R}[m_x^1 + 2 : m_x^1 + m_x^2 + 3] = \mathbf{W}_x^{-1} \cdot \hat{\mathbf{F}}[m_x^1 + 2 : m_x^1 + m_x^2 + 3] \\
&\vdots \\
\tilde{\mathbf{G}}^{N_s} \cdot [\mathbf{W}_y^1]^{\mathrm{T}} &= \mathbf{R}[2N_x + 1 - l_x^{N_s} + 1 : 2N_x + 1] \\
&= \mathbf{W}_x^{-1} \cdot \hat{\mathbf{F}}[2N_x + 1 - l_x^{N_s} + 1 : 2N_x + 1],
\end{aligned} \tag{51}$$

Thus one finds $\tilde{\mathbf{G}}^i$ by inverting $[\mathbf{W}_y^i]^{\mathrm{T}}$ in the ith sub-block of Eq. (50).

Remark 5. One can formulate the above procedure such that one inverts $\mathbf{W}_y$ first instead of $\mathbf{W}_x$. Then the condition of $(m_y^1 + 1) + (m_y^2 + 1) + \cdots + (m_y^{N_s} + 1) = 2N_y + 1$ will be imposed. Recall that one can first determine the resolution, i.e., m_x^i or m_y^i and then let $2N_x + 1 = \sum_{i=1}^{N_s} (1 + m_x^i)$ or $2N_y + 1 = \sum_{i=1}^{N_s} (1 + m_y^i)$.

Remark 6. It is obvious that $\mathbf{W}_x$ in the above can be easily singular since there exists a non-zero constant α such that $W_x^i = \alpha W_x^j$ for $i \neq j$ if the x interval of the ith and jth sub-domains are identical.

4.2.2. Inverse Reconstruction of 2D Sliced Fourier Image

Due to the possible singular properties and the complexity of $\mathbf{W}_x$ or $\mathbf{W}_y$, we reconstruct $f(x, y)$ slice-by-slice instead of domain-by-domain, that is, *we seek $f(x, y)$ at a given $y = y_0$ (or $x = x_0$) reducing the problem to the 1D reconstruction problem and then apply the IPRM. We then collect all $f(x, y_0)$ (or $f(x_0, y)$) and patch them together for the reconstruction of $f(x, y)$.*

At a certain point $y = y_0$, the Fourier approximation is given by

$$\begin{aligned}
f_N(x, y_0) &= \sum_{k_x=-N_x}^{N_x} \sum_{k_y=-N_y}^{N_y} \hat{f}_{k_x k_y} \exp(\mathrm{i} k_x \pi x) \exp(\mathrm{i} k_y \pi y_0) \\
&\equiv \sum_{k=-N_x}^{N_x} \hat{p}_k \exp(\mathrm{i} k \pi x),
\end{aligned} \tag{52}$$

where $\hat{p}_k$ are the Fourier coefficients of the 1D function $f_N(x, y_0)$ given by

$$\hat{p}_k = \sum_{k_y=-N_y}^{N_y} \hat{f}_{kk_y} \exp(ik_y \pi y_0). \tag{53}$$

Let each subdomain in the x-direction at $y = y_0$ be denoted by $\omega_x^i(y = y_0)$. Then with the IPRM, we seek a one-dimensional piecewise smooth function $h(x, y_0)$ which is the reconstruction of $f_N(x, y)$ at $y = y_0$ such that

$$(h(x, y_0), \exp(\mathrm{i}k\pi x))_F = \hat{p}_k, \tag{54}$$

Here $h(x, y_0)$ is

$$h(x, y_0) = \bigoplus_{i=1}^{N_s^x(y_0)} \left(\sum_{l=0}^{m_x^i} \tilde{g}_l^i C_l^\lambda(X_i(x)) \right), \tag{55}$$

where $N_s^x(y_0)$ is the number of sub-domains at $y = y_0$ in the x-direction and m_x^i is the highest expansion mode in ω_x^i. Using Eq. (54) we find $\tilde{g}_l^i$. We note that $\tilde{g}_l^i$ has a dependence on y, i.e., $\tilde{g}_l^i = \tilde{g}_l^i(y)$ since $h(x, y_0)$ is a reconstruction of $f_N(x, y_0)$ only in the x-direction. Now we seek a one-dimensional piecewise smooth function $\tilde{h}(x_0, y)$ which is the reconstruction of $h(x, y)$ at $x = x_0$ such that

$$\tilde{h}(x_0, y) = \bigoplus_{j=1}^{N_s^y(x_0)} \sum_{l=0}^{m_y^j} \tilde{r}_l^j C_l^\lambda(Y_j(y)), \tag{56}$$

where $N_x^y(x_0)$ is the number of sub-domains at $x = x_0$ in the y-direction, m_y^j is the highest expansion mode in $\omega_y^j(x = x_0)$ and $\tilde{r}^j$ is the expansion coefficients in $\omega_y^j(x = x_0)$. Here $\omega_y^j(x = x_0)$ is jth subdomain at $x = x_0$ in the y-direction. In order to apply the inverse method, the Fourier coefficients of $h(x_0, y)$ which are denoted by $\hat{q}_k$ should be calculated. By definition

$$(h(x_0, y), \exp(\mathrm{i}k\pi y))_F = \hat{q}_k. \tag{57}$$

Using the above equation, we have that

$$\hat{q}_k = \frac{1}{2} \int_{-1}^{1} \left(\bigoplus_{j=1}^{N_s^y(x_0)} z^j(x_0, y) \right) \exp(-\mathrm{i}k\pi y) dy, \tag{58}$$

where

$$z^j(x_0, y) = \sum_{l=0}^{m_x^i(y)} \tilde{g}_l^i(y) C_l^\lambda(X_i(x_0)), \quad x_0 \in \omega_x^i(y), \quad y \in \omega_y^j(x_0). \tag{59}$$

and $z^j(x_0, y)$ can be evaluated via DFT. The collection of $\tilde{h}(x_0, y)$ for all x_0 forms the final inverse reconstruction $\tilde{f}_m(x, y)$, that is,

$$\tilde{f}_m(x, y) = \tilde{h}(x, y). \tag{60}$$

Remark 7. If $f(x, y)$ is a piecewise polynomial, the inverse reconstruction slice-by-slice is exact.

First we show that if $f(x, y)$ is a polynomial in a given domain the inverse method with the slice-by-slice technique is equivalent to the 2D global inverse method and thus it is exact. Let $f(x, y)$ be a polynomial of degree $(m+n)$ such that

$$f_{mn}(x, y) = \sum_{l_x=0}^{m} \sum_{l_y=0}^{n} g_{l_x l_y} C_{l_x}^\lambda(x) C_{l_y}^\lambda(y). \tag{61}$$

In the previous section, we showed that the global inverse method is exact if $f(x, y)$ is a polynomial in Eq. (27) and its reconstructed function has coefficients given by Eq. (24). Thus, we have that,

$$\tilde{f}(x, y) = \sum_{l_x=0}^{m} \sum_{l_y=0}^{n} \left(\mathbf{W}_x^{-1} \cdot \hat{\mathbf{F}} \cdot \mathbf{W}_y^{\mathrm{T}^{-1}} \right)_{l_x l_y} C_{l_x}^\lambda(x) C_{l_y}^\lambda(y). \tag{62}$$

The inverse method slice-by-slice is equivalent to Eq. (62).

Consider the inverse reconstruction of Eq. (61). At $y = y_0$, the inverse reconstruction $h(x, y_0)$ is given by

$$h(x, y_0) = \sum_{l_x=0}^{m} \tilde{g}_{l_x}^x(y_0) C_{l_x}^\lambda(x), \tag{63}$$

where $\tilde{g}_{l_x}^x$ are the expansion coefficients in the x-direction at $y = y_0$. Let $\tilde{\mathbf{g}}^x = (\tilde{g}_0^x, \ldots, \tilde{g}_m^x)^{\mathrm{T}}$. Then from Eq. (13) we obtain

$$\tilde{\mathbf{g}}^x = \mathbf{W}_x^{-1} \cdot \hat{\mathbf{f}}^x, \tag{64}$$

where we note that $\mathbf{W}_x$ and $\hat{\mathbf{f}}^x$ are functions of y and $\hat{\mathbf{f}}^x$ is the column vector composed of the Fourier coefficients at $y = y_0$. Then we obtain

$$\begin{aligned}\tilde{g}_{l_x}^x(y_0) &= \sum_{k_x=-N}^{N} \left(\mathbf{W}_x^{-1}\right)_{l_x k_x} \hat{f}_{k_x}^x \\ &= \sum_{k_x=-N}^{N} \left(\mathbf{W_x}^{-1}\right)_{l_x k_x} \sum_{k_y=-M}^{M} \hat{f}_{k_x k_y} \exp(\mathrm{i}k_y \pi y_0) \\ &= \sum_{k_y=-M}^{M} \left(\sum_{k_x=-N}^{N} \left(\mathbf{W_x}^{-1}\right)_{l_x k_x} \hat{f}_{k_x k_y} \right) \exp(\mathrm{i}k_y \pi y_0), \end{aligned} \tag{65}$$

where $N = \frac{m}{2}$ and $M = \frac{n}{2}$ for the invertibility. We rewrite Eq. (63) in the form

$$h(x_0, y) = \sum_{l_x=0}^{m} \tilde{g}_{l_x}^x(y) C_{l_x}^{\lambda}(x_0),$$

and use Eq. (65) to get,

$$h(x_0, y) = \sum_{k_y=-M}^{M} \exp(\mathrm{i}k_y \pi y) \left(\sum_{l_x=0}^{m} C_{l_x}^{\lambda}(x_0) \sum_{k_x=-N}^{N} \left(\mathbf{W}^{\mathbf{x}-1}\right)_{l_x k_x} \hat{f}_{k_x k_y} \right). \tag{66}$$

As we see in the above equation, we know that $h(x_0, y)$ is a partial Fourier sum in the y-direction. Thus the Fourier coefficients in the y-direction at $x = x_0$ are

$$\hat{f}_{k_y}^y = \sum_{l_x=0}^{m} C_{l_x}^{\lambda}(x_0) \sum_{k_x=-N}^{N} \left(\mathbf{W}_x{}^{-1}\right)_{l_x k_x} \hat{f}_{k_x k_y}. \tag{67}$$

Let $\tilde{h}(x_0, y)$ be the inverse reconstruction of $h(x_0, y)$ such that

$$\tilde{h}(x_0, y) = \sum_{l_y=0}^{n} \tilde{g}_{l_y}^y C_{l_y}^{\lambda}(y), \tag{68}$$

and by the definition of the inverse method

$$\tilde{g}_{l_y}^{y} = \sum_{k_y=-M}^{M} \left(\mathbf{W}_y^{-1}\right)_{l_y k_y} \hat{f}_{k_y}^{y}$$
$$= \sum_{k_y=-M}^{M} \left(\mathbf{W}_y^{-1}\right)_{l_y k_y} \left(\sum_{l_x=0}^{m} C_{l_x}^{\lambda}(x_0) \sum_{k_x=-N}^{N} \left(\mathbf{W}_x{}^{-1}\right)_{l_x k_x} \hat{f}_{k_x k_y} \right). \quad (69)$$

Thus at $(x, y) = (x_0, y_0)$, the final inverse reconstruction is

$$\tilde{h}(x_0, y_0) = \sum_{l_y=0}^{n} \tilde{g}_{l_y}^{y}(x_0) C_{l_y}^{\lambda}(y_0)$$
$$= \sum_{l_y=0}^{n} \sum_{k_y=-M}^{M} \left(\mathbf{W}_y{}^{-1}\right)_{l_y k_y} \left(\sum_{l_x=0}^{m} C_{l_x}^{\lambda}(x_0) \sum_{k_x=-N}^{N} \left(\mathbf{W}_x{}^{-1}\right)_{l_x k_x} \hat{f}_{k_x k_y} \right) C_{l_y}^{\lambda}(y_0)$$
$$= \sum_{l_x=0}^{m} \sum_{l_y=0}^{n} \left(\mathbf{W}_x^{-1} \cdot \hat{\mathbf{F}} \cdot \mathbf{W}_y^{\mathrm{T}-1} \right)_{l_x l_y} C_{l_x}^{\lambda}(x_0) C_{l_y}^{\lambda}(y_0). \quad (70)$$

Thus, by comparison with Eq. (62),

$$\tilde{h}(x_0, y_0) = \tilde{f}(x_0, y_0). \quad (71)$$

Now consider the case that $f(x, y)$ is a piecewise polynomial. Suppose that the given domain is composed of subdomains Ω^i and let the polynomial function inside each subdomain be denoted by $f^i(x, y)$ such that

$$f_{m_i n_i}^{i}(x, y) = \sum_{l_x=0}^{m_i} \sum_{l_y=0}^{n_i} g_{l_x l_y}^{i} C_{l_x}^{\lambda}(X_i(x)) C_{l_y}^{\lambda}(Y_i(y)), \quad (x, y) \in \Omega^i. \quad (72)$$

At $y = y_0$, the Fourier coefficients $\hat{\mathbf{f}}_{k_x}^{x}$ in the x-direction are

$$\hat{f}_{k_x}^{x}(y_0) = \sum_{k_y=-M}^{M} \hat{f}_{k_x k_y} \exp(\mathrm{i} k_y \pi y_0). \quad (73)$$

Then the inverse reconstruction at $y = y_0$ is given by

$$h(x, y_0) = \bigoplus_{i=1}^{N_s^x(y_0)} z^i(x, y_0), \quad (74)$$

where $N_s^x(y_0)$ is the number of subdomains in the x-direction at $y = y_0$. And $z^i(x, y_0)$ is given by

$$z^i(x, y_0) = \sum_{l_x=0}^{p_i} \tilde{g}_{l_x}^i(y_0) C_{l_x}^{\lambda}(X(x)), \tag{75}$$

where p_i is

$$p_i = m_j \quad \text{if} \quad (x, y_0) \in \Omega^j. \tag{76}$$

Here we note that p_i can be greater than m_j as $\tilde{g}_{l_x}^i = 0$ for $l_x > m_j$. From Eqs. (13) and (73), the expansion coefficients are given by

$$\tilde{g}_{l_x}^i = \sum_{k_x=-N}^{N} \left(\mathbf{W}_x{}^{-1}\right)_{l_x k_x} \hat{f}_{k_x}^x, \tag{77}$$

where $\mathbf{W}_x$ is defined as in Eq. (41) such as $\mathbf{W}_x = [\mathbf{W}_x^1(y_0)| \cdots |\mathbf{W}_x^{N_s^x}(y_0)]$, and

$$l = \begin{cases} l_x & \text{if} \quad i = 1 \\ (i-1)(p_i+1) + l_x & \text{otherwise} \end{cases} \tag{78}$$

In order to find what the function $h(x, y_o)$ in Eq. (74) represents, consider a function $g(x, y_o)$ given by

$$g(x, y_o) = \sum_{k_y=-M}^{M} \left(f(x, y), \exp(\mathrm{i}k_y \pi y)\right)_F \exp(\mathrm{i}k_y \pi y_o), \tag{79}$$

where $f(x, y)$ is the original piecewise polynomial function. $g(x, y_0)$ is a sliced function of $g(x, y)$ which is the Fourier representation of $f(x, y)$ only in the y-direction. Thus the Gibbs oscillations exist only in the y-direction while its functional form in the x-direction is same as that of $f(x, y)$. Since there are $N_s^x(y_0)$ subdomains in the x-direction at $y = y_0$, $g(x, y_0)$ in Eq. (79) can be rewritten as

$$g(x, y_0) = \bigoplus_{i=1}^{N_s^x(y_0)} v^i(x, y_0), \tag{80}$$

where

$$v^i(x, y_0) = \sum_{l_x=0}^{p_i} g_{l_x}^i(y_0) C_{l_x}^{\lambda}(X(x)). \tag{81}$$

Since the 1D multidomain inverse method is exact when the function is a piecewise polynomial, $g_{l_x}^i$ is equivalent to the expansion coefficients by the inverse method, that is,

$$\mathbf{g}(y_0) = \mathbf{W}_x^{-1}(y_0) \cdot \hat{\mathbf{q}}(y_0), \tag{82}$$

where $\mathbf{W}_x, \hat{\mathbf{q}}$ and $\mathbf{g}$ are

$$\begin{aligned} \mathbf{W}_x &= [\mathbf{W}_x^1(y_o) | \cdots | \mathbf{W}_x^{N_s^x(y_0)}] \\ \hat{q}_{k_x} &= (g(x, y_0), \exp(\mathrm{i}k_x \pi x))_F \\ \mathbf{g} &= (g_0^1, \cdots, g_{p_1}^1, \cdots, g_0^{N_s^x(y_0)}, \cdots, g_{p_{N_s^x(y_0)}}^{N_s^x(y_0)}). \end{aligned} \tag{83}$$

From Eq. (79),

$$\begin{aligned} \hat{q}_{k_x} &= \sum_{k_y=-M}^{M} \left(\left(f(x, y), \exp(\mathrm{i}k_y \pi y) \right)_F, \exp(\mathrm{i}k_x \pi x) \right)_F \exp(\mathrm{i}k_y \pi y_0) \\ &= \hat{\mathbf{f}}_{k_x}. \end{aligned} \tag{84}$$

Thus from Eqs. (77) and (82), we know that,

$$\tilde{g}_{l_x}^i = g_{l_x}^i, \tag{85}$$

and

$$h(x, y_0) = g(x, y_0). \tag{86}$$

Now in the same manner, the inverse reconstruction $\tilde{h}(x, y)$ of $h(x, y)$ in the y-direction is equivalent to the inverse Fourier transformation of $g(x, y_0)$ in the y-direction, that is,

$$\tilde{h}(x, y) = f(x, y). \tag{87}$$

Thus the inverse reconstruction slice-by-slice is exact if the function $f(x, y)$ is a piecewise polynomial.

Example 2. In order to show the exactness of the inverse reconstruction, we consider a piecewise constant function for the simplicity such as

$$f(x,y)=\begin{cases}0.1 & \text{for } \Omega_1=[-1,0]\times[0,1]\\ 0.31 & \text{for } \Omega_2=[0,1]\times[0,1]\\ 0.53 & \text{for } \Omega_3=[-1,0]\times[-1,0]\\ 0.68 & \text{for } \Omega_4=[0,1]\times[-1,0].\end{cases} \tag{88}$$

It is obvious that $\mathbf{W}_x^1=\mathbf{W}_x^3$ and $\mathbf{W}_y^1=\mathbf{W}_y^2$ and thus $\mathbf{W}_x$ or $\mathbf{W}_y$ is a singular matrix. We use again the exact Fourier coefficients for this example which are given by

$$\hat{f}_{k_xk_y}=\begin{cases}0 & \text{if } k_x=\text{even} \quad \text{or } k_y=\text{even}\\ \frac{-2.4}{40\pi^2k_xk_y} & \text{if } k_x=\text{odd} \quad \text{and } k_y=\text{odd}\\ \frac{16i}{40\pi k_y} & \text{if } k_x=0 \quad \text{and } k_y=\text{odd}\\ \frac{-7.2i}{40\pi k_x} & \text{if } k_x=\text{odd} \quad \text{and } k_y=0\\ \frac{16.2}{40} & \text{if } k_x=0 \quad \text{and } k_y=0.\end{cases} \tag{89}$$

To illustrate the methodology, we assume that we know the exact discontinuity locations and that we know the original piecewise function is a 2D step function. By the second assumption, we let m_x and m_y be zero – one can also use the residue technique [30] to determine the resolution. Then by the first step of the IPRM and with the 1D Fourier coefficients $\hat{p}_k$ at $y=y_0$, $\tilde{g}_0^{\mathrm{l}}$, and $\tilde{g}_0^{\mathrm{r}}$ are given by the following

$$\begin{bmatrix} W_{x\,00}^{\mathrm{l}} & W_{x\,00}^{\mathrm{r}} \\ W_{x\,10}^{\mathrm{l}} & W_{x\,10}^{\mathrm{r}} \end{bmatrix}\begin{bmatrix}\tilde{g}_0^{\mathrm{l}}\\ \tilde{g}_0^{\mathrm{r}}\end{bmatrix}=\begin{bmatrix}\hat{p}_0\\ \hat{p}_1\end{bmatrix}, \quad \text{at } y=y_0, \tag{90}$$

where the superscripts l and r denote the left and right domain at $y=y_0$. With the definition of $\mathbf{W}$ and the given interval,

$$\begin{bmatrix}\tilde{g}_0^{l}\\ \tilde{g}_0^{r}\end{bmatrix}=\begin{bmatrix}1 & -\frac{i\pi}{2}\\ 1 & \frac{i\pi}{2}\end{bmatrix}\begin{bmatrix}\sum_{k_y=-N_y}^{N_y}\hat{f}_{0k_y}\exp(\mathrm{i}k\pi y_0)\\ \sum_{k_y=-N_y}^{N_y}\hat{f}_{1k_y}\exp(\mathrm{i}k\pi y_0)\end{bmatrix}, \quad \text{at } y=y_0. \tag{91}$$

Now we obtain $h(x,y)$ for all y. Again note that $h(x,y)$ still exhibits Gibbs oscillations in the y-direction. We have

$$h(x_0, y) = \tilde{g}_0(y) = \sum_{k_y=-N_y}^{N_y} \left(\hat{f}_{0k_y} - \frac{i\pi}{2} \hat{f}_{1k_y} \right) \exp(\mathrm{i}k_y \pi y), \tag{92}$$

for $x = x^l$ or

$$h(x_0, y) = \tilde{g}_0(y) = \sum_{k_y=-N_y}^{N_y} \left(\hat{f}_{0k_y} + \frac{i\pi}{2} \hat{f}_{1k_y} \right) \exp(\mathrm{i}k_y \pi y), \tag{93}$$

for $x = x^{\mathrm{r}}$. Thus the new Fourier coefficients $\hat{q}_{k_y}$ of $h(x_0, y)$ are

$$\hat{q}_{k_y} = \begin{cases} \hat{f}_{0k_y} - \frac{i\pi}{2} \hat{f}_{1k_y} & \text{for } x = x^l \\ \hat{f}_{0k_y} + \frac{i\pi}{2} \hat{f}_{1k_y} & \text{for } x = x^r \end{cases} \tag{94}$$

Since we assume that we know $m_y = 0$, the inverse method for the final reconstruction $\tilde{h}(x_0, y)$ is given by

$$\begin{bmatrix} \tilde{g}_0^b \\ \tilde{g}_0^{\mathrm{T}} \end{bmatrix} = \begin{bmatrix} 1 & -\frac{i\pi}{2} \\ 1 & \frac{i\pi}{2} \end{bmatrix} \begin{bmatrix} \hat{q}_0 \\ \hat{q}_1 \end{bmatrix}, \quad \text{at } x = x_o, \tag{95}$$

where the superscripts b and t denote the bottom and top domains and $\hat{q}_0$ and $\hat{q}_1$ are with Eq. (94) given by

$$\hat{q}_0 = \begin{cases} \hat{f}_{00} - \frac{i\pi}{2} \hat{f}_{10} & \text{for } x = x^l \\ \hat{f}_{00} + \frac{i\pi}{2} \hat{f}_{10} & \text{for } x = x^r \end{cases}, \tag{96}$$

and

$$\hat{q}_1 = \begin{cases} \hat{f}_{01} - \frac{i\pi}{2} \hat{f}_{11} & \text{for } x = x^l \\ \hat{f}_{01} + \frac{i\pi}{2} \hat{f}_{11} & \text{for } x = x^r. \end{cases} \tag{97}$$

In Fig. 2 the Fourier image $f_N(x, y)$ and the reconstructed image $\tilde{f}_m(x, y)$ of $f(x, y)$ are shown. Clearly the wiggly patterns in the neighborhood of the interior boundaries and the domain boundaries are considerably reduced. Indeed by the inverse method the reconstruction is exact as shown in Table II.

In the above example, we use the fact that function in each subdomain is a constant function, that is, we use that $m = 0$ for all subdomains. Since the inverse method is exact, the maximum errors reach machine accuracy if $m = 0$ as shown in the table. However, one can choose any m

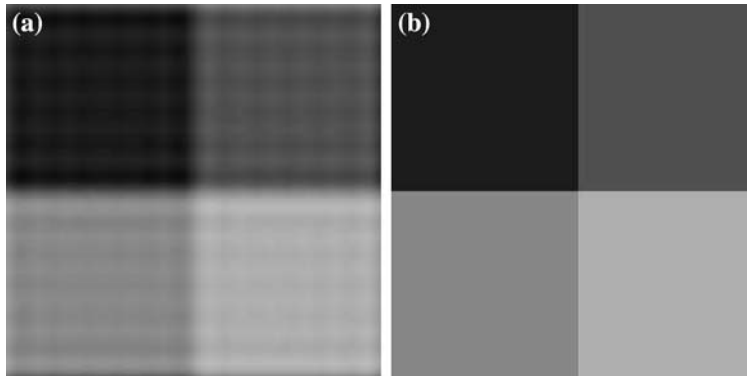

Fig. 2. $f_N(x, y)$ and $\tilde{f}_m(x, y)$ for Example 2, Eq. (88): (a) the Fourier image of $f(x, y)$ with $N_x = N_y = 12$. (b) the reconstructed image of $f(x, y)$ with $N_x = N_y = 1$ and $m_x = m_y = 0$.

Table II. Example 2, Eq. (88): Absolute Maximum Error of $\tilde{f}_m(x, y)$ by the Inverse Method with $N_x = N_y = 1$ with $m_x = m_y = 0$

Ω_i	$E(x, y)$
Ω_1	2.7756E-17
Ω_2	0
Ω_3	1.1102E-16
Ω_4	0

instead of $m = 0$. The maximum errors then increase, which is not due to the approximation errors but due to the round-off errors.

5. LOCAL RECONSTRUCTION OF THE SHEPP–LOGAN PHANTOM IMAGE

In the previous section, we considered the two dimensional reconstruction problem with the IPRM for a problem which has a simple geometry and whose exact Fourier coefficients are known. If the geometry of sub-domains is simple, calculating the transformation matrix **W** is relatively easy. However, in most cases the geometry of the sub-domains is complex and the Fourier coefficients are given based only on a discrete grid. Thus we use DFT or other integration methods to evaluate the Fourier coefficients and the transformation matrix **W**. Other than that, the 2D IPRM can be applied in exactly the same manner as described in the previous sections to more realistic and complicated problems.

In this section, we reconstruct the well-known medical image, the Shepp-Logan phantom image that is widely used as a benchmark for image reconstruction algorithms [24,29]. The Shepp-Logan phantom image is composed of ten ellipses each of which has different major and minor axis with different rotation angle filled by a single gray level. The sub-components made by the multiple overlaps of these ten ellipses are represented by a single gray scale, that is, the 2D function representing the Shepp-Logan phantom image is a piecewise constant function. The sharp boundaries between the sub-components are the jumps of the function and yield the Gibbs oscillations when reconstructed in the Fourier series. To reduce the oscillations, the various filtering techniques are usually used [24,28]. The Gegenbauer reconstruction method has been also successfully applied to the Shepp-Logan phantom image [1,2] with high accuracy.

The Shepp–Logan phantom image used in this work is obtained from the MATLAB® built-in function, $f = phantom\ ('modified Shepp - Logan')$. A MATLAB® built-in 2D FFT subroutine, *fft2* is also used to find the Fourier coefficients and its image. In Fig. 3 the original Shepp-Logan phantom and its Fourier image are shown on the grids $257 \times 257 = [0, 2\pi] \times [0, 2\pi]$ with $N_x = N_y = 128$. As shown in the figure, the Fourier image shows the Gibbs oscillations over the entire domain.

Applying the IPRM to the phantom image can be done in the same manner and is straightforward as explained in the previous examples, but there are issues involved that should be addressed before applying the method.

(1) Edge detection problem: as shown in the figure there are many discontinuities over the domain and the exact locations of these discontinuities or edges should be found first. In this work we do not intend to employ any edge detection algorithm to find these edges but instead we assume that the exact edge locations are known a priori from the discrete grid points. However, of course, it must be noted that the convergence of the method can be affected by the order of the edge detection algorithm used. Since the image is given on the discrete grid points, the exact location of the edge should not necessarily be on a grid point. Thus if the exact location is off-grid, the calculation of the transformation matrix $\mathbf{W}$ is undetermined and $\mathbf{W}$ can be different depending on the definition of the edge. (2) Singular property of $\mathbf{W}$: it is usual that the edges are so closely clustered that the transformation matrix can be ill-posed in such cases. In general the image is given on the finite set of grid points and thus it is possible for a particular sub-domain to contain a small number of points, such that the transformation matrix results is a singular matrix. To avoid this, one can either ignore that particular sub-domain and consider it as a part of the neighboring domains or use more off-grid points to construct

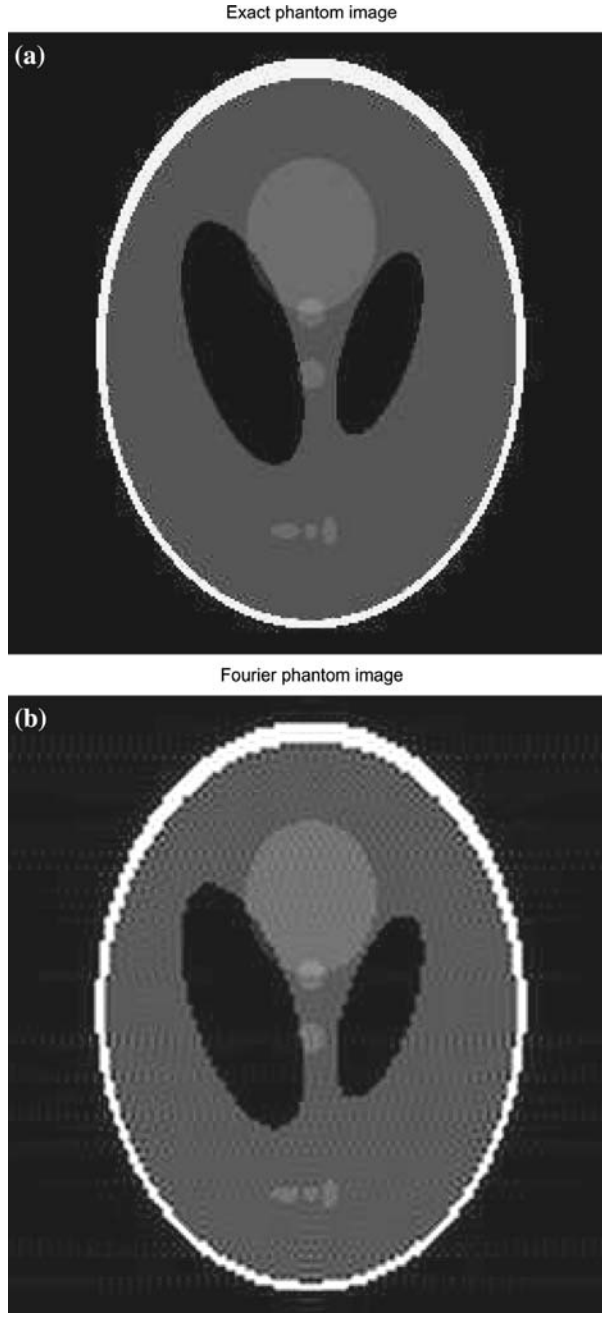

Fig. 3. Shepp-Logan phantom image f(x,y). (a) the exact image f_{exact} (b) the Fourier image f_N with $N_x = N_y = 128$.

a non-singular **W**. However, excluding such sharp edges by even one grid point can be easily detected by eye. (3) The integration for **W**: contrary to the continuous case, the numerical integration is needed for the integration of **W**. In this work, we use the Gauss quadrature rule as well as DFT [6]. In the previous paper [23], we discussed the effect on the reconstruction of different integration algorithms for $\hat{f}_k$ and **W**. If the Fourier coefficients are obtained by using the DFT then using **W** calculated by the DFT gives better results than using **W** by the quadrature rules and vice versa.

In this work, we determine the edge location as the mid point of the two different neighboring sub-domains. Moreover we assume that we know that each sub-component is represented as a constant function, that is, it has a single valued gray scale. We first recontruct the image in the x-direction and then in the y-direction followed by the procedure discussed in the previous section. As mentioned earlier, we know the edge locations of the piecewise constant function. Since the image function is a piecewise constant function, we know that $m_x = 0$ and $m_y = 0$. In future work, we will discuss the effects arising when the above assumptions are removed and the reconstruction with the IPRM is carried out more realistically.

The results are shown in Figs. 3–6. In Fig. 3, the exact phantom image and its Fourier image with $N_x = N_y = 128$ are shown. As shown in the figure, the Fourier image shows the Gibbs oscillations due to the multiple jumps over the entire domain. In Fig. 4, the phantom image with the IPRM is shown. As shown in the figure, the IPRM reconstructs the 2D image with high accuracy.

In Fig. 5, we show a sliced image located at $y = 5.0560$, which is composed of 11 sub-domains. The 4th to the 8th domains are very closely clustered as shown. Due to the complexity of this slice, the maximum error is relatively greater than that of the other sliced images where the domain geometry is relatively well defined and thus the absolute maximum error is much smaller. Fig. 6a shows the exact image of the sliced image, Fig. 6b shows the Fourier image and Fig. 6c shows the image reconstructed with the IPRM. As shown in the figure the inverse method shows good agreement in this slice. The results show that the IPRM reconstructs the image accurately even in the complex regions where the edges are clustered.

6. SUMMARY

In this work, we have applied the inverse polynomial reconstruction method (IPRM) to the 2D image reconstruction with the goal of resolving the Gibbs oscillations of the Fourier image. The 2D global and local IPRM have been presented and shown that the 2D IPRM yields higly accu-

Fig. 4. The inverse image f_N with $N_x = N_y = 128$.

Fig. 5. The location of the sliced image at $y = 5.0560$ (solid line).

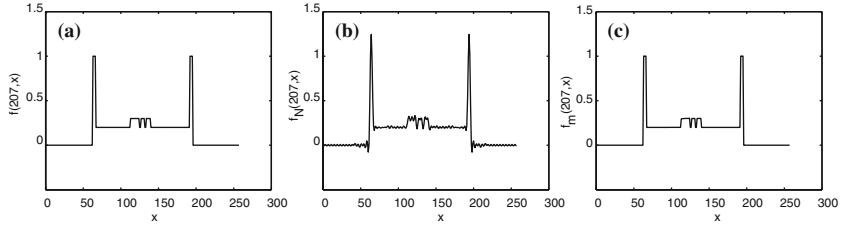

Fig. 6. Sliced Shepp–Logan phantom image at $y = 5.0560$. (a) the exact sliced image of $f(x, y)$ (b) the Fourier sliced image of $f_N(x, y)$ (c) the inverse sliced image of $\tilde{f}_m(x, y)$.

rate results. It is also shown that the 2D IPRM is exact when the image is a piecewise polynomial as previously demonstrated for the 1D IPRM. The Shepp–Logan phantom image is reconstructed with the 2D IPRM and it is shown that the reconstruction is done accurately. The edge locations are assumed as known quantities in this work so that the edge effect is minimized. The current work has shown that the 2D IPRM provides a robust and efficient and also accurate image reconstruction algorithm.

ACKNOWLEDGEMENTS

This research is supported by a grant to BDS from the Natural Science and Engineering Research Council of Canada. JHJ is on PIMS postdoctoral fellowship at the University of British Columbia, Vancouver, BC, Canada. The authors thank Dr. Wai-Sun Don and Dr. Misun Min for helpful discussions.

REFERENCES

1. Archibald, R., and Gelb, A. (2002). Reducing the effects of noise in image reconstruction. *J. Sci. Comp.* **17**, 167–180.
2. Archibald, R., Chen, K., Gelb, A., and Renaut, R. (2003). Improving tissue segmentation of human brain MRI through pre-processing by the Gegenbauer reconstruction method. *Neuroimage*, to appear.
3. Bateman, H. (1953). *Higher Transcendental Functions*, Vol. 2, McGraw-Hill, New York.
4. Canuto, C., Hussaini, M. Y., Quarteroni, A., and Zang, T. A. (1988). *Spectral Methods in Fluid Dynamics, Springer Series in Computational Physics*, Springer, New York.
5. Chen, H., and Shizgal, B.D. (2001). A spectral solution of the Sturm-Liouville equation: comparison of classical and nonclassical basis sets, *J. Comp. Appl. Math.* **136**, 17–35.
6. Davis, P.J., and Rabinowitz, P. (1989). *Methods of Numerical Integration*, Academic Press, New York.
7. Driscoll, T.A., and Fornberg, B. (2001). A Padé-based algorithm for overcoming the Gibbs phenomenon, *Numerical Algorithms* **26**, 77–92.
8. Ekstrom, M.P. (1984). *Digital Image Processing Techniques, Computational Techniques*, vol. 2, Academic Press, Orlando.

9. Feichtinger, H.G., and Strohmer, T. (2001). Numerical Harmonic Analysis and Image Processing, in Kropatsch, W. G., and Bischof, H.(eds.), *Digital Image Analysis*, Springer-Verlag, New York, 7–47.
10. Gautschi, W. (1985). *J. Comp. Appl. Math.* **12**, pp.61–76.
11. Gelb, A., and Gottlieb, D. (1997). The resolution of the Gibbs phenomenon for "sliced" functions in one and two dimensions. *Comp. Math. Appl.* **33**, 35–38.
12. Golub, G.H., and Van Loan, C.F. (1996). *Matrix Computations*, 3rd Ed., Johns Hopkins UP, Baltimore.
13. Gonzalez, R.C., and Woods, R.E. (1992). *Digital Image Processing*, Addison-Wesley Publishing.
14. Gottlieb, D., and Hesthaven, J. S. (2001). Spectral methods for hyperbolic problems. *J. Comp. Appl. Math.* **128**, 83–131.
15. Gottlieb, D., and Orszag, S. (1977). *Numerical Analysis of Spectral Methods: Theory and Applications*, SIAM, Philadelphia.
16. Gottlieb, D., and Shu, C.-W. (1997). On the Gibbs phenomenon and its resolution. *SIAM Rev*. **39**, 644–668.
17. Gottlieb, D., Shu, C.-W., Solomonoff, A., and Vandeven, H. (1992). On the Gibbs phenomenon I: Recovering exponential accuracy from the Fourier partial sum of a nonperiodic analytic function. *J. Comput. Appl. Math.* **43**, 81–92.
18. Gottlieb, D., and Tadmor, E. (1985). Recovering pointwise values of discontinuous data within spectral accuracy. In Progress and Supercomputing in Computational Fluid Dynamics, Murman, E.M., and Abarbanel, S.S.(eds), Proceedings of 1984 U.S.-Israel Workshop, Progress in Scientific Computing, vol. 6, Birkhauser, Boston, 357–375.
19. Gradshteyn, I. S., and Ryzhik, I. M. (200). *Table of Integrals, Series, and Products*, 6th Ed., Academic Press, San Diego.
20. Green, W. B. (1989). *Digital Image Processing: A Systems Approach*, 2nd Ed., Van Nostrand Reinhold, New York.
21. Hord, R. M. (1982). *Digital Image Processing of Remotely Sensed Data*, Series of Notes and Reports in Computer Science and Applied Mathematics, Academic Press, New York.
22. Hu, M.-K. (1962). Visual pattern recognition by moment invariants, *IRE Trans. on Information Theory IT-8*, 179–187.
23. Jung, J.-H., and Shizgal, B. D. (2004). Generalization of the inverse polynomial reconstruction method in the Resolution of the Gibbs Phenomena. *J. Comp. Appl. Math.* **172**, 131–151.
24. Kak, A. C. (1984). Image reconstruction from projections. In Digital Image Processing Techniques, Ekstrom, M.P.(ed.) Academic Press, New York, 111–170.
25. Lanczos, D. (1996). *Discourse on Fourier series*, Hafner Publishing Company, New York.
26. Oppenheim, A. V., Wilsky, A. S., and Nawab, S. H. (1996). *Signals and Systems*, 2nd Ed., Prentice Hall, New Jersey.
27. Pratt, W. K. (1991). *Digital Image Processing*, 2nd Ed., John Wiley and Sons, New York.
28. Rowland, S. W. (1979). Computer Implementation of Image Reconstruction Formulas. In Image Reconstruction from Projection, Herman, G. T. (ed.), Topics in Applied Physics, Vol. 32, Springer-Verlag, New York, 9–79.
29. Shepp, L. A., and Logan, B. F. (1974). The Fourier reconstruction of a head section. *IEEE Trans. Nucl. Sci. NS.* **21**, 21–43.
30. Shizgal, B. D., and Jung, J.-H. (2003) Towards the resolution of the Gibbs phenomena. *J. Comp. Appl. Math.* **161** 41–65.
31. Tadmor, E., and Tanner, J. (2002). Adaptive mollifiers for high resolution recovery of piecewise smooth data from its spectral information. *Found. Comp. Math.* **2**, 155–189.